

Article

Formation of Noble Metal Phases (Pt, Pd, Rh, Ru, Ir, Au, Ag) in the Process of Fractional Crystallization of the CuFeS₂ Melt

Elena Fedorovna Sinyakova ^{1,*}, Inga Grigorievna Vasilyeva ², Aleksandr Sergeevich Oreshonkov ^{3,4},
Sergey Vladimirovich Goryainov ¹ and Nikolay Semenovich Karmanov ¹

- ¹ V.S. Sobolev Institute of Geology and Mineralogy, Siberian Branch of the Russian Academy of Sciences, pr. Akademika Koptyuga 3, 630090 Novosibirsk, Russia
- ² Nikolaev Institute of Inorganic Chemistry, Siberian Branch of the Russian Academy of Sciences, Ac. Lavrentieva ave. 3, 630090 Novosibirsk, Russia
- ³ Laboratory of Molecular Spectroscopy, Kirensky Institute of Physics, Federal Research Center KSC SB RAS, Akademgorodok 50/38, 660036 Krasnoyarsk, Russia
- ⁴ School of Engineering and Construction, Siberian Federal University, 660041 Krasnoyarsk, Russia
- * Correspondence: efsin@igm.nsc.ru

Abstract: The quasi-equilibrium directional crystallization of the melt composition (at. %): Cu 24.998, Fe 25.001, S 49.983, with Ag 0.002, Pd 0.003, Ru 0.004, Rh 0.006, and Au, Pt, Ir (each as 0.001) was carried out. The crystallized cylindrical ingot consisted of two primary zones and three secondary zones with different chemical and phase compositions. The compositions of the primary zones corresponded to high-temperature intermediate solid solution (zone I) and liquid enriched in sulfur (zone II). The compositions of the secondary zones corresponded to low-temperature intermediate solid solution and chalcopyrite (zone Ia), the same intermediate solid solution with chalcopyrite and bornite (zone Ib), and again with bornite, chalcocite, and idaite (zone II). We plotted the distribution curves of Fe, Cu, and S along the ingot, calculated the distribution coefficients of the components during directional crystallization, and clearly showed that, from the initial stoichiometric composition CuFeS₂, the intermediate solid solution enriched in Fe and depleted in S is crystallized. Based on the data of directional crystallization and thermal analysis, a cross section was constructed in the intermediate solid solution-sulfide melt region of the Cu-Fe-S system. With solubility in the solid Cu-Fe sulfides lying below detection limit of scanning electron microscopy/energy-dispersive X-ray spectrometry (SEM/EDS), noble elements occurred as individual phases of a size more often <10 μm. They were identified as Ag, RuS₂, PdS, Au* (an Au based alloy), (Rh, Ir, Ru)₃S₈, (Rh, Ir)₃S₈, Rh₃S₈, and (Cu, Fe)₂(Pt, Rh)₁S₅ phases by electron microprobe. Based on ab initio calculations of crystal structure, electronic band structure, and lattice dynamics of idealized laurite RuS₂ phase and the idealized Ir₃S₈, Rh₃S₈, and Ru₃S₈ phases, the interpretation of Raman spectrum of the cation-mixed (Ru, Rh, Ir)₂S₂ sulfide was presented for the first time.

Keywords: Cu-Fe-S system; noble metals; directional crystallization; intermediate solid solution; fine inclusions



Citation: Sinyakova, E.F.; Vasilyeva, I.G.; Oreshonkov, A.S.; Goryainov, S.V.; Karmanov, N.S. Formation of Noble Metal Phases (Pt, Pd, Rh, Ru, Ir, Au, Ag) in the Process of Fractional Crystallization of the CuFeS₂ Melt. *Minerals* **2022**, *12*, 1136. <https://doi.org/10.3390/min12091136>

Academic Editor: Gianfranco Ulian

Received: 6 August 2022

Accepted: 2 September 2022

Published: 7 September 2022

Publisher's Note: MDPI stays neutral with regard to jurisdictional claims in published maps and institutional affiliations.



Copyright: © 2022 by the authors. Licensee MDPI, Basel, Switzerland. This article is an open access article distributed under the terms and conditions of the Creative Commons Attribution (CC BY) license (<https://creativecommons.org/licenses/by/4.0/>).

1. Introduction

Knowledge of equilibrium phase diagrams of the Cu-Fe-S system and transition processes between phases is important information for geology, and a large body of data about the phase diagram of this system is known. In the central zone of the liquidus surface of the diagram, there are fields of the pyrrhotite solid solution Fe_zCu_{1-z}S_{1+y}, intermediate solid solution (Cu, Fe)_{S_{1-x}}, and bornite solid solution Cu_{5±x}Fe_{1±x}S_{4±y} [1–6]. These high-temperature solid solutions have wide regions of homogeneity. The possibility of crystallization from a melt of both stoichiometric CuFe₂S₃ isocubanite and copper-enriched Cu_{1.1}Fe_{2.0}S_{3.0} isocubanite was shown in [7,8]. Most of the problems are associated with (Cu, Fe)_{S_{1-x}}, which crystallizes at a temperature of 960 °C by the reaction between

$\text{Fe}_z\text{Cu}_{1-z}\text{S}_{1\pm y}$ and a copper-rich sulfide melt [3]. High-temperature isothermal sections in the middle part of the solid-melting diagram of the Cu-Fe-S system show the intermediate solid solution crystallization region without equilibria of the sulfide melt with another ternary intermediate phase [3,4,6]. There is a lack of data on the positions of conodes during the crystallization of this solid solution in a wide range of temperature and melt composition variations. Limited quantitative data on the equilibrium distribution coefficients of the components are available in the works [3,4,6,8,9]. Stable and metastable modifications of *Iss* were obtained by directed crystallization of melts with compositions lying in the regions of primary crystallization of intermediate and pyrrhotite solid solutions, and each modification had its own field on the liquidus surface and showed different behavior upon cooling [9]. The study of a series of isothermal sections of the phase diagram showed that $(\text{Cu, Fe})\text{S}_{1-x}$ cooled to room temperature decomposes with the formation of chalcopyrite group minerals [3–5,10]. This decay is controlled by kinetics and, therefore, there is a large uncertainty in the identification of sulfide associations in the subsolidus range. Metastable states are best understood if their ideal equilibrium state is known. In this case, directional crystallization as a process with the most favorable kinetics, combined with a detailed study of the chemical and microstructural features of a crystallized ingot, is the best way to supply data on the equilibrium state of the sulfide associations.

The chalcopyrite group minerals forming typical associations of copper-rich sulfide Cu-Ni ores are characterized by high contents of precious metals [11–16]. Some data on the behavior of noble metal in the region of intermediate solid solution and melt coexistence were obtained under isothermal conditions [16–21] and by fractional crystallization of the melt [22–26]. It should be noted that most of these elements are present as inclusions of native metals, alloys, intermetallic compounds, sulfides, or compounds with chalcophile elements (Te, As, Bi, and Sb) between the basic sulfides, whereas data on the content of these elements in the basic sulfides very scant. It is known that even small amounts of impurity atoms have an influence on the nucleation rate, through creating some stresses interacting with vacancies in the lattice [27]. Therefore, it is necessary to control the real distribution of the impurity elements, both in matrix sulfides and in micro-inclusions of small sizes.

The transformation of chalcopyrite composition during the quasi-directional crystallization was performed previously [9]. The aim of this work was to study a fragment of the phase diagram of the Cu-Fe-S system in the region of crystallization of an intermediate solid solution, and to identify the forms of precipitation of noble metal minerals during fractional crystallization of a CuFeS_2 melt. To do so, the following operations were planned: plotting of trajectories of the melt composition changes and intermediate solid solution as well as a fan of conodes on the concentration triangle and constructing a polythermal section of the melting diagram of the Cu-FeS system along the $(\text{Cu, Fe})\text{S}_{1-x}$ crystallization path; determination of the amount of noble metals in the matrix sulfides and in fine inclusions by electron beam probe analysis using scanning and point variants, and employing the entire arsenal of statistical expedients and standard practices for providing trustworthy final results; characterization of complex-mixed inclusions with size $< 1 \mu\text{m}$ and polyphasic aggregates by Raman spectroscopy, which is highly valuable for the identification of the nature of such types of phases.

To facilitate the manuscript reading, acronyms of the most-used abbreviators are provided below:

- *Iss* intermediate solid solution $(\text{Cu, Fe})\text{S}_{1\pm x}$;
- *Bnss* bornite solid solution $\text{Cu}_{5\pm x}\text{Fe}_{1\pm x}\text{S}_{4\pm y}$;
- *L* sulfide liquid;
- *Ls* liquid rich in sulfur;
- *Cp^f* $\text{Cu}_{0.98}\text{Fe}_{1.03}\text{S}_{1.98}$ phase closed to tetragonal chalcopyrite;
- *Iss^t* low-temperature tetragonal intermediate solid solution;
- *Chc* chalcocite Cu_2S ;
- *Bn* bornite Cu_5FeS_4 ;
- *Id* idaite Cu_5FeS_6 .

2. Experimental Section

2.1. Procedures

The initial sample of the composition (at. %): Cu 24.998, Fe 25.001, S 49.983, Ag 0.002, Pd 0.003, Ru 0.004, Rh 0.006, Au, Pt, Ir (0.001 each) was prepared from metals (99.99%) and sulfur (99.9999%), and purified of moisture by vacuum distillation. The basic principles of synthesis and directed crystallization are provided in [23]. The mixture of elements in a given ratio was held in a quartz ampoule under vacuum of 1.5×10^{-2} Pa at 1050 °C for a day, and then cooled in air. After crushing, a powder (about 11 g) was placed in a vacuumed and sealed ampoule with an inner diameter of about 8 mm and conical bottom, which was located in a vacuumed quartz container ~10 mm in diameter. Directional crystallization was carried out by the Bridgman-Stockbarger method in a two-zone furnace, where the sample in the upper zone was heated to full melting and kept for two days, cooling was into the cold zone at a speed of $2.25 \cdot 10^{-8}$ m/s. It should be noted that such a regime provided quasi-equilibrium conditions during the directional crystallization, which made it possible to use the experimental results for the study of phase equilibria in the Cu-Fe-S system. Temperatures of 905 °C and 534 °C were recorded at the beginning and end of crystallization in the lower end of the quartz ampoule. After the completion of crystallization, the ampoule was cooled in the switched-off furnace. The ingot cooled to room temperature was dense, its tail part was swollen, and some drops of sulfur were observed on the ampoule walls.

2.2. Characterization

2.2.1. SEM/EDS

The crystallized ingot, about 90 mm long and about 8 mm in diameter, was cut perpendicular to the longitudinal axis into 30 pieces; each was weighed and determined the fraction (*g*) of the crystallized melt. Fifteen polished pieces were used to obtain information on microstructure, phase, and chemical composition and thermochemical properties. The average compositions of matrix sulfides and fine individual inclusions were determined by scanning electron microscopy with energy-dispersive X-ray spectrometry, using a high-resolution microscope MIRA 3 LMU (Tescan Orsay Holding, Brno, Czechia) equipped with X-ray microanalysis system AZtec Energy XMax 50 (Oxford Instruments Nanoanalysis Ltd., High Wycombe, UK) at the Analytical Center for multi-elemental and isotope research SB RAS (Novosibirsk, Russia). The measurements were made at electron beam energy of 20 keV and current of 1.5 nA, live spectrum acquisition time was 30 s (total square of spectrum about 6×10^5 counts). In this case, area of the X-ray generation zone (spatial resolution of the analysis) was 2–3 μm with a beam spot size of 8–9 nm. The X-ray intensity of the *K*-family S, Fe, and Cu and *L*-family Ru, Rh, Pd, Ag, Ir, Pt, and Au was also used. As standards, pure metals and FeS₂ for sulfur were used. The detection limit for the elements was 0.1–0.5 wt. % with accuracy of 1%. Phases smaller than 5 μm were analyzed with a point probe. The average composition of multiphase regions was determined by scanning an area of up to 1 mm², and to reduce the detection limit by approximately 2 times, the acquisition time of spectra was increased to 120 s. The average composition of phase mixtures was calculated from 3–5 analyzes from different sites of interest from each section along the ingot. Although such a method for analyzing multiphase objects from the point of view of classical electron probe microanalysis seems to be not quite correct, nevertheless, the relative error in determining the main components in such samples does not actually exceed 1–2%, as was shown previously [28].

The sulfide matrix contained many inclusions of noble metal microphases with a size of up to 0.5 μm. To determine their composition, the region of generation of X-ray radiation with an energy of beam electrons of 20 keV exceeds the size of inclusions; therefore, the spectra of such inclusions are largely contaminated by the radiation of host matrix components. Therefore, to increase the reliability of identification of fine mineral phases, we carried out a series of measurements at an electron beam energy of 10 keV. At this energy, the size of the X-ray generation zone decreases by about four times. Unfortunately,

reducing the energy of the electron beam to 10 keV did not allow us to significantly improve the accuracy of the analysis, since we had to use the intensity of *M*-families Ir, Pt, and Au as analytical radiation, the deconvolution of the spectra of which is not performed reliably enough by the software. In addition, the efficiency of excitation of Cu *K*-families' lines is too low, and the error of matrix corrections for the Cu *L*-family intensity is very large.

The average composition values along the length of a cylindrical solid ingot c_i^s were used to construct the dependence of the component concentrations on each fraction g of the crystallized melt. The composition of the melt at an arbitrary moment of crystallization c_i^l was calculated based on these data and the material balance equation:

$$c_i^l = \frac{c_{i0} - \int_0^g c_i^s dg}{1 - g} \quad (1)$$

Here, c_{i0} is the concentration (in at. %) of the i -th component in the initial ingot. It can be used for calculating the distribution coefficient of a component between crystal and melt $k_i(g) = c_i^s/c_i^l$.

2.2.2. Thermal Analysis

When a solid solution crystallizes from a melt, analysis of a directionally crystallized sample demonstrates the compositional change of the solid and liquid phases during crystallization [29]. A series of samples whose compositions are located at the points of the trajectory of the change in the melt composition was prepared and studied by differential thermal analysis (DTA), and due to these results, a segment lying on the liquidus surface in the region of solid solution crystallization was constructed. A curvilinear section of the melting diagram along the crystallization path was designed, due to the combining of DTA and directional crystallization data. A thermal experiment was carried out as derivative thermal analysis (DDTA), recording the dependence of the change rate of the temperature difference between standard and sample on time, and fixing more clearly the onset of melt crystallization [30]. Samples of given compositions weighing ~0.2 g were specially synthesized from elements in special thermo analytical quartz ampoules 3–4 mm in diameter evacuated to a residual pressure of 1.5×10^{-2} Pa with a concave bottom. The melting points of the samples were determined by standardless thermal analysis, heating the sample at a rate of 15 deg/min, and cooling at a rate of ~30 deg/min. The coordinates of thermal effects were found from the results of automatic differentiation of temperature–time curves. The thermocouple was tested by the melting point of gold. The error of recording the melting temperature was ± 5 °C.

2.2.3. XRD

For four samples finely ground with $g = 0.09, 0.21, 0.37,$ and 0.53 , XRD measurements were carried out using a Dron-4 diffractometer (Bourestnik JSC, Saint-Petersburg, Russia) with Cu $K\alpha$ radiation and C monochromator over a 2-theta range of 25–80° with 1° step. Lines of intensity of about 1–2% were accessible for observation. The obtained diffraction patterns were interpreted using Powder Diffraction File, Inorganic Index, International Center for Diffraction Data File (Pennsylvania, U.S.A). This method successfully characterized the matrix sulfides, other than micro inclusions, that were present in low concentration [27]. Therefore, the Raman technique was used to obtain structural information for them.

2.2.4. Raman Spectroscopy

Here, Raman spectroscopy was used to characterize inclusions of Ru-Rh-Ir sulfides with size of ~60 μm based on the Raman spectroscopic data bank RRUFF [31]. The Raman spectra were recorded with Horiba Jobin Yvon LabRAM HR800 spectrometer (Kyoto, Japan) [32–34] excited with 532-nm green line of a Thorlabs Nd:YAG laser (40-mW power, working at double-harmonic frequency). The power of incident light was attenuated by optical filters to about 1 mW. The back-scattered light was collected with an Olympus

objectives at magnification of $50\times$ ($WD = 0.4$ mm) and $100\times$ ($WD = 0.2$ mm). The spectra were accumulated with a 1024-channel Peltier-cooled CCD detector in the region from 70 to 3800 cm^{-1} . The use of uniform $100\text{ }\mu\text{m}$ slit and pinhole at holographic grating of 1800 grooves/mm provided the 2.2 cm^{-1} resolution. Ne lamp lines were used for spectral calibration. The deconvolution of Raman spectra into Voigt amplitude contours was performed with the Model S506 Interactive PeakFit software (2002 Spectroscopy Software, Canberra Industries, Meriden, CT, United States) [35]. AutoFit Peaks II Second derivative method of this software was selected using minimization by least squares, sparse by root-finding, vary the bandwidth, with linear background and maximum iterations of 50.

Calculation of lattice dynamics and Raman spectra simulation were done using density function theory (DFT [36–38]) formalism implemented in CASTEP code [39]. The local density approximation [40] was used. Initial structures of investigated compounds were totally optimized using the following convergence conditions: 5.0×10^{-6} eV/atom for energy, 0.01 eV/Å for maximum force, and 0.02 GPa for maximum stress. The norm-conserving pseudopotentials with a cutoff energy equal to 720 eV were used. The actual spacing for Monkhorst-Pack grid over Brillouin zone was no more than 0.05 1/Å . The Lorentzian smearing equal to 5, 20 and 30 cm^{-1} was tested for Raman spectra plotting. The phonon dispersion calculations for RuS_2 along high symmetry directions of the BZ was performed using a linear response formalism [41].

3. Results and Discussion

3.1. Behavior of Macrocomponents

3.1.1. Chemical Composition

Results of the crystallization process as photographs of the crystallized ingot and images of parts from different zones are shown in Figure 1.

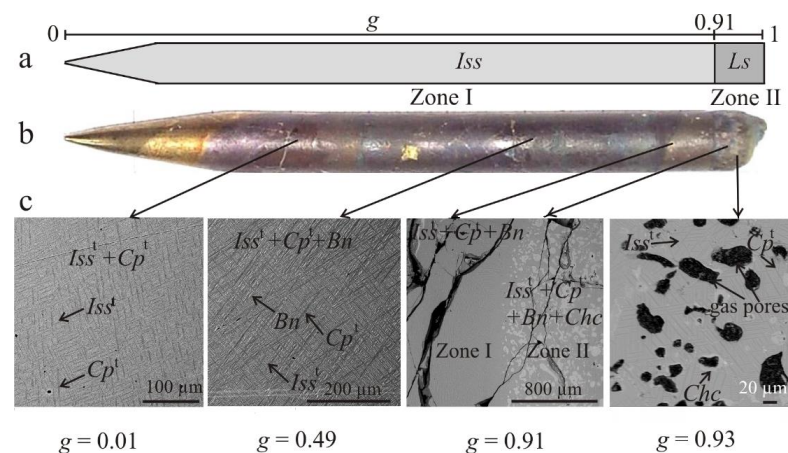


Figure 1. Scheme of primary zoning of a directionally crystallized ingot (a), photograph of ingot (b), and back-scattered electron images of sulfides in the secondary zones (c). Black areas are cracks and pores.

Identification of primary phases and reconstructs of the primary phase zoning were made based on values of average composition in cross sections of the ingot, taking into account the known data on high-temperature phases in the Cu-Fe-S system. The ingot consists of two primary zones: zone I ($0 \leq g \leq 0.91$) occupies the larger part of the ingot, and here, *I_{ss}* crystallizes from the melt; in zone II ($0.91 \leq g \leq \sim 1$), *L_s* is formed (Figure 1a). In Table 1, quantitative compositional variations of both of these states and their distribution coefficients are shown as the function of *g* varying up to = 0.8.

These data were transformed into the distribution curves of the main components along the ingot and into the curve of change in the melt composition (Figure 2). From this figure it follows that, during crystallization, Fe predominantly passes into *I_{ss}* ($k_{\text{Fe}} = 1.2\text{--}1.6$), while *L* becomes enriched in sulfur ($k_{\text{S}} = 0.98\text{--}0.85$) and copper ($k_{\text{Cu}} = 0.88\text{--}0.97$). With increase of sulfur in the melt, the distribution coefficients of Cu and Fe increase, while k_{S} decreases.

Table 1. Composition of *Iss*, *L*, and distribution coefficients of components between *Iss* and *L* (*k*) depending on the degree of crystallization (*g*).

<i>g</i>	Composition of <i>Iss</i> (at. %)			Composition of Melt (at. %)			<i>k</i> (<i>Iss/L</i>)		
	Fe	S	Cu	Fe	S	Cu	Fe	S	Cu
0.04	29.07	48.87	22.06	24.83	50.05	25.12	1.17	0.98	0.88
0.06	28.93	48.32	22.75	24.74	50.08	25.17	1.17	0.96	0.90
0.09	28.73	48.73	22.54	24.61	50.13	25.26	1.17	0.97	0.89
0.13	28.24	49.08	22.68	24.44	50.18	25.38	1.16	0.98	0.89
0.16	28.69	48.41	22.90	24.29	50.24	25.47	1.18	0.96	0.90
0.19	28.38	48.63	22.99	24.14	50.30	25.56	1.18	0.97	0.90
0.22	28.36	48.64	23.00	23.98	50.36	25.66	1.18	0.97	0.90
0.32	28.09	48.43	23.48	23.37	50.68	25.95	1.20	0.96	0.90
0.37	28.06	48.54	23.40	23.00	50.85	26.15	1.22	0.95	0.89
0.46	27.85	47.82	24.33	22.19	51.36	26.45	1.26	0.93	0.92
0.53	26.84	48.79	24.37	21.45	51.74	26.81	1.25	0.94	0.91
0.56	26.92	48.02	25.06	21.07	52.00	26.93	1.28	0.92	0.93
0.59	26.49	48.10	25.41	20.68	52.28	27.04	1.28	0.92	0.94
0.73	25.83	47.91	26.26	17.70	54.56	27.74	1.46	0.88	0.95
0.77	25.41	47.58	27.01	16.36	55.77	27.87	1.55	0.85	0.97

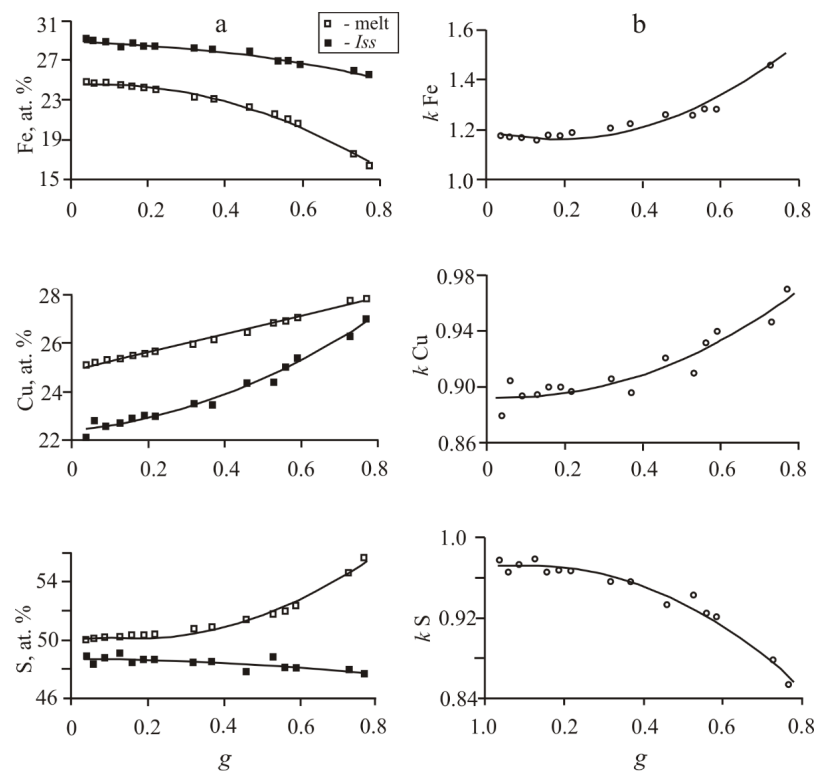


Figure 2. Distribution curves of Fe, Cu, and S in zone I of directly crystallized sample (a). Dependence of distribution coefficient of Fe, Cu, and S between *Iss* and melt on the fraction of crystallized melt *g* (b).

3.1.2. Crystallization Paths

In Figure 3, trajectories of changes in the composition *L* as AB and that in *Iss* as CD, together with the fan of conodes, are plotted on the concentration triangle, based on results from Table 1. This clearly demonstrates the behavior of the Cu-Fe-S system during fractional crystallization.

One can see that the first portions of *Iss* in the ingot had the composition Fe_{0.29}Cu_{0.22}S_{0.49} enriched in Fe and depleted in S relative to the initial melt; the composition shifts towards Cu and becomes even more depleted in sulfur (at *g* = 0.77 it is Fe_{0.25}Cu_{0.27}S_{0.48}) as the degree of crystallization *g* increases.

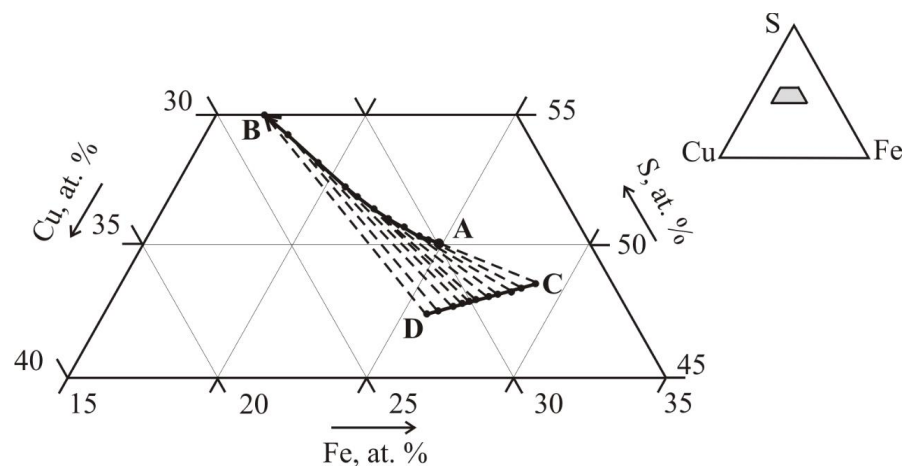


Figure 3. Displaying results of directional crystallization on the composition triangle.

A is initial melt, AB is the change path in the melt composition during the *I_{ss}* formation, CD is the trajectory of the *I_{ss}* composition change, AC is the conode at the beginning moment of crystallization; and BD is the conode at $g \sim 0.8$; the arrow shows the direction of change in the melt composition, dashed lines show the transformation of conodes during crystallization.

Based on the scheme of the liquidus surface [2] during directional crystallization, most of the part of the tested ingot should consist of *I_{ss}* and a liquid enriched with sulfur, when the trajectory reaches the separation region. As crystallization proceeds, the amount of sulfide liquid *L* decreases until it disappears completely, and at the end, a sequence of numerous reactions should realize with the formation of a multiphase product and porous inclusions of gaseous sulfur. The result obtained in our experiment and shown in Figure 3 corresponds well to such a scenario.

In the process of the crystallization of *I_{ss}*, in the melt the sulfur concentration increases, while in *I_{ss}* it decreases. Similar behavior was noted during the crystallization of ternary Cu-Fe-S melts as in [9], where our measured values of the distribution coefficients of the main components between *I_{ss}* and *L* agree with their data. This means that macrocomponents behave in strict accordance with the theory of quasi-equilibrium directional crystallization, the main regularities of which were formulated previously on the example of Fe-Ni-S and Cu-Fe-S systems in [42].

3.1.3. Polythermal Section

These foregoing results were supplemented with data of the derivative thermal analysis of four samples, whose compositions lie on the trajectory of the change in the composition melt. A polythermal cross section of the phase diagram of the Cu-Fe-S system was built using the directional crystallization and thermal analysis of specially synthesized samples along the crystallization path (Figure 4). Since the *I_{ss}* + *L* conodes are located on this surface, this section shows the conditions of phase equilibrium along the crystallization path. This approach was also successful in constructing different quasi-binary sections of the Cu-Fe-S system along the crystallization paths, such as stoichiometric CuFe_2S_3 and non-stoichiometric $\text{Cu}_{1.1}\text{Fe}_{1.9}\text{S}_3$ phases [7,8], a section of the Fe-Ni-S diagram in the region of successive crystallization of two solid solutions [43] and sections of the Cu-Fe-Ni-S diagram describing the crystallization of a monosulfide solid solution [44], and in the region of successive crystallization of four solid solutions [45].

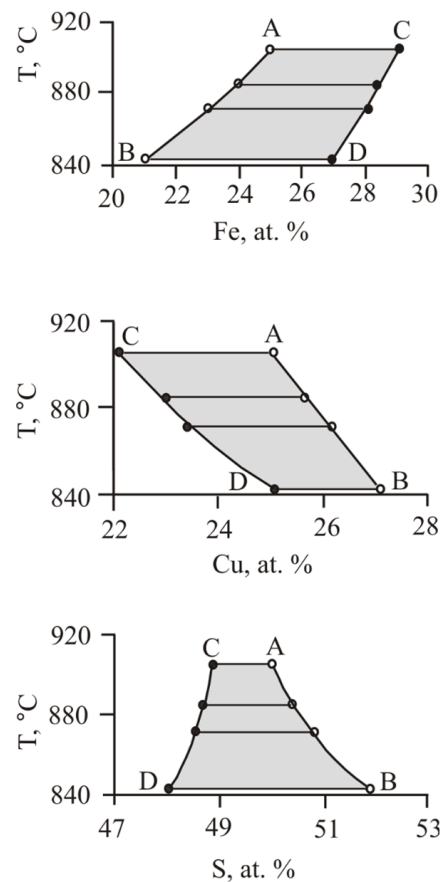


Figure 4. Polythermal section of the Cu-Fe-S phase diagram along the crystallization path in the *Iss* crystallization region. AB is liquidus line, and CD is solidus line.

3.1.4. Microstructure

With decreasing temperature, in a directionally crystallized ingot, subsolidus phase reactions become possible, and this leads to the occurrence of inclusions in one of the primary phases, or to its complete decomposition into daughter phases. In this case, separation of the primary zones into secondary zones happens. Therefore, for the ingot consisting of two primary zones: $(\text{Cu, Fe})\text{S}_{1-x}$ and *Ls* shown in Figure 1a, zone I is divided into two subzones according to the phase associations formed due to decay of *Iss* (Figure 1c). The microstructure of subzone Ia at $0 \leq g \leq \sim 0.5$ is matrix *Iss^t* of the composition $\text{Cu}_{4.3}\text{Fe}_{4.6}\text{S}_{8.1}$, in which lamellas of tetragonal *Cp^t* phases with the cell parameters as $a = 5.304 \pm 0.001$ (2) Å, $c = 10.425 \pm 0.002$ (3) Å and $a = 5.318 \pm 0.006$ (2) Å, $c = 10.424 \pm 0.050$ (3) Å are presented (Figure 1c, $g = 0.01$, Table 2). Based on the relation of the strong diffraction peaks intensity, the amounts of the *Iss^t* and *Cp^t* phases are about the same, and it is difficult to establish which phase is breaking up. In addition, difficulties arise in the differentiation of microcrystalline phases chemically and structurally close to each other, which are the decay products of *Iss* or other non-quenching Fe-Cu sulfides in the Cu-Fe-S system. Identification of these types of samples requires a more sensitive and precise diffraction technique, such as that which was used in [46]. In subzone Ib ($\sim 0.5 \leq g \leq 0.91$), in addition to these phases, micron-sized bornite inclusions occur (Figure 1c, $g = 0.49$). The diffraction peak at $d = 1.937$ Å with intensity of $I/I_0 = 2$ was detected in the samples with $g = 0.49$ and 0.73 (Table 2), and was related to the strongest peak of cubic bornite, according to data [47]. These results are consistent with those in [6], where at temperature below 500 °C, the stability of sulfide associations such as $\text{Cp} + \text{Iss}$ and $\text{Cp} + \text{Iss} + \text{Bn}$ is confidently shown. At the end of this zone, a sharp change in microstructures occurs (Figure 1c, $g = 0.91$). Table 2 demonstrates the reliability of the identification of the decay products from zone I.

Table 2. Identification of the decay products of *Iss* from zone I according to XRD standards.

Experimental Samples										PDF Card			
<i>g</i> = 0.09		<i>g</i> = 0.21		<i>g</i> = 0.37		<i>g</i> = 0.49		<i>g</i> = 0.73		270164, <i>Iss</i> ^t		090423, <i>Cp</i> ^t	
<i>d</i> (Å)	<i>I</i> / <i>I</i> ₀	<i>d</i> (Å)	<i>I</i> / <i>I</i> ₀	<i>d</i> (Å)	<i>I</i> / <i>I</i> ₀	<i>d</i> (Å)	<i>I</i> / <i>I</i> ₀	<i>d</i> (Å)	<i>I</i> / <i>I</i> ₀	<i>d</i> (Å)	<i>I</i> / <i>I</i> ₀	<i>d</i> (Å)	<i>I</i> / <i>I</i> ₀
3.058	88	3.079	86	3.075	85	3.075	59	3.068	100	3.08	100	3.03	100
3.003	100	3.058	100	3.057	100	3.054	100	3.056	95			2.89	10
2.66	6	2.66	7	2.661	8	2.65	6	2.65	8	2.66	30	2.64	30
2.61	2	2.62	2	2.626	3	2.62	2	2.62	1			2.60	10
						1.937	2	1.943	2			2.30	10
1.876	39	1.883	44	1.878	45	1.886	36	1.873	53	1.88	80		
		1.879	44	1.876	39	1.875	47			1.870	20		
1.862	32	1.866	31	1.863	34	1.863	37	1.859	26			1.852	80
		1.862 [?]	25									1.867	40
1.602	17	1.555	20	1.602	15	1.602	17			1.610	60		
1.596	22	1.550	21	1.598	16	1.596	23	1.593	18	1.590	10	1.590	60

Zone II ($0.91 \leq g \leq \sim 1$) consists of several products crystallizing from the liquid enriched in sulfur: Cu_5FeS_4 , low-temperature *Iss*^k of composition $\text{Cu}_{28.3}\text{Fe}_{23.6}\text{S}_{48.1}$, tetragonal CuFeS_2 , chalcocite Cu_2S , idaite Cu_5FeS_6 , and porous inclusions of gaseous sulfur, which condensed on the walls of the ampoule when the sample was cooled to room temperature. Gas pores are often contoured by chalcocite (Figure 1c, $g = 0.93$). We did not study this area in more detail.

3.2. Behavior of Microcomponents

3.2.1. Chemical Composition and Microstructure

According to available data in the literature, Pt and Au do not accumulate in *Iss* [17,18], Rh dissolves in sulfur-rich *Iss* [48], and Pd can enter *Iss* where $\text{Cu}/\text{Fe} > 1$ [18]. We can assert with reasonable justification that the solubility of noble metals in the *Iss* matrix is below the detection limit of X-ray microanalysis, and during the melt crystallization, the formation of its own phases of noble metals is the preferential process. Based on Figures 5 and 6, and Table 3, the following phases were identified chemically: RuS_2 , $(\text{Rh}, \text{Ir}, \text{Ru})_3\text{S}_8$, $(\text{Rh}, \text{Ir})_3\text{S}_8$, and Rh_3S_8 phases compositionally close each to other, PdS, Ag, an alloy based on Au which we have designated as Au^* , and $(\text{Cu}, \text{Fe})_{-2}(\text{Pt}, \text{Rh})_1\text{S}_{-5}$ phase enriched in Cu and Pt. Note that all these phases crystallize at different stages of melt solidification. Some words about their distribution:

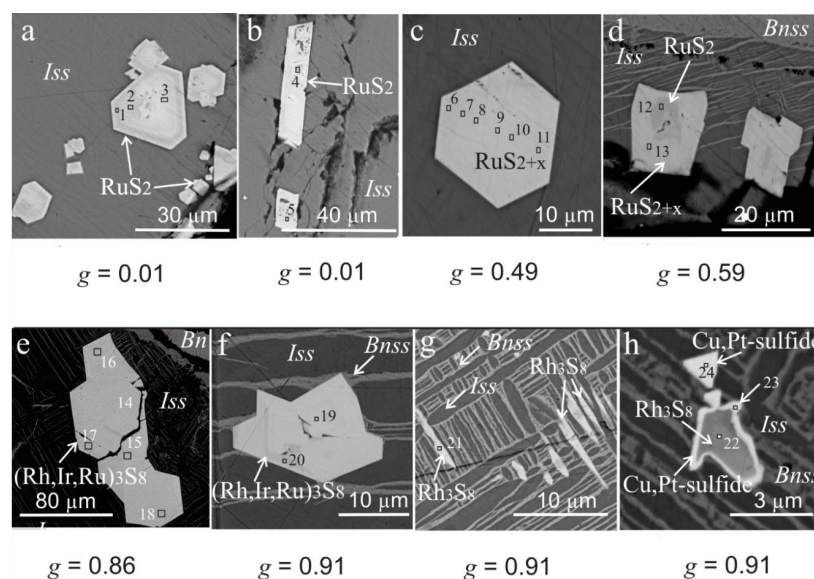


Figure 5. SEM images (a–h) of noble metal phases microstructures in sulfide matrices in back-scattered electrons. Numbers 1–24 indicate locations of X-ray spectral microanalyses (for values, see Table 3).

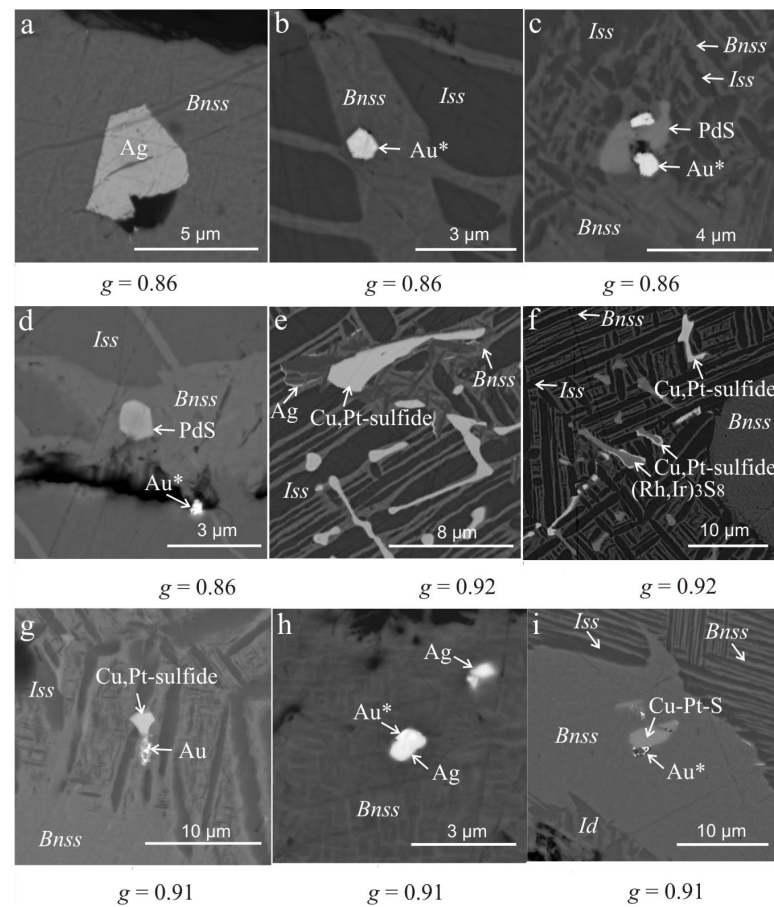


Figure 6. SEM images (a–i) of Au, Ag, Pt, Pd, and Rh phases microstructures in sulfide matrices in back-scattered electrons.

Ru, Rh, Ir. Most parts of the ruthenium are released from the melt as RuS_2 at the initial moment of crystallization at $0 \leq g \leq 0.01$ (Figure 5a,b). The refractory ruthenium sulfide laurite RuS_2 with $T_m \sim 1600^\circ\text{C}$ is known from the Ru-S binary system [49]. In the *Iss* matrix, RuS_2 crystals present as single-phase inclusions up to $60\ \mu\text{m}$ and as aggregates with each other. They are characterized by a distinct cut, mainly in the form of hexagons (Figure 5a), and less often in the form of tablets (Figure 5b). Other forms of RuS_2 crystals contain impurities Ir, Rh, Fe, and Cu, as seen in Table 3. In these crystals, spatial chemical inhomogeneity is observed: their central zone is rich in ruthenium, while the rim zone is enriched in iridium. The Ru remaining in the melt is crystallized as a unit of rare single RuS_2 crystals up to $g \sim 0.86$. With g increasing, the sulfur concentration in the Ru-crystals increases (Table 3, No. 6–13). There are both the compositionally homogeneous RuS_{2+x} inclusions, able to dissolve about 6 Ir, 3 Rh, 3 Fe, and 1 Cu (in at. %) (Figure 5c, Table 3, No. 6–11), and compositionally zonal inclusions (Figure 5d, Table 3, No. 12, 13). The core of the zoned inclusions is represented by stoichiometric RuS_2 with a small admixture of Ir and Rh (about 1 at. %), the outer part is enriched in sulfur and impurities of Ir and Rh—about 4 and 3%, respectively. According to the mineralogical data [50], natural laurite can dissolve about 11 wt. % Ir and 2 wt. % Rh. In [51,52], experiments studying the influence of temperature and active sulfur $f(\text{S}_2)$ on the phase relations in the Ru-Os-Ir-Cu-S system showed that laurite RuS_2 can crystallize from the melt at temperatures of $1200\text{--}1250^\circ\text{C}$ together with Ir, and the Ir solubility increases with increasing $f(\text{S}_2)$: at 1250°C and $f(\text{S}_2) 10^{-0.07}$, the Ir content increases to ~ 12 at. %. Despite the low content of ruthenium in the initial melt, conditions for the formation of individual RuS_2 crystals from the melt in our experiment were most likely fulfilled at a temperature of about 905°C , which corresponds to the beginning of melt crystallization in the experiment. Apparently, RuS_2 nuclei appear

in the surface layer of the melt and are captured by growing *Iss* crystals. Clusters of RuS_2 are present in the *Iss* matrix at the edges of the section (Figure 5a). Previously, we observed a similar behavior of RuS_2 crystals during melt solidification in the Cu-Fe-Ni-S-(Ru, Rh) system at the beginning of pyrrhotite crystallization [46]. In both cases, RuS_2 crystals are collected in the conical part of the ampoule. In [46], it was suggested that the conical shape of the RuS_2 sediment may be associated with Marangoni convection directed from bottom to top along the walls of the ampoule. This causes a radial movement of the melt, directed from the center of the crystallization front to its edges. From a melt rich in sulfur (55.77 at. %) and copper (atomic ratio Cu/Fe = 1.7), at $g \geq 0.86$, a phase compositionally close to (Rh, Ir, Ru) $_3\text{S}_8$ crystallizes. This forms large aggregates or intergrowths ranging from $10 \times 20 \mu\text{m}$ to $60 \times 70 \mu\text{m}$ distributed in the matrix *Iss* + *Bnss* (Figure 5e,f), which, apparently, crystallized from the melt.

Table 3. Chemical characterization of microstructural noble metal phases by SEM/EDS¹.

N	Formula	Photo Evidence	Fe	Cu	Ag	Pt	Pd	Ru	Ir	Rh	S	Total
1	RuS_2	Figure 5a	5.17	2.57	0.39	<LD ²	<LD	44.91	9.55	2.02	37.85	102.45
			5.06	2.21	0.20	<LD	<LD	24.27	2.71	1.07	64.48	
2	RuS_2		2.19	0.88	<LD	<LD	<LD	50.97	7.63	2.18	37.95	101.8
			2.18	0.77	<LD	<LD	<LD	27.99	2.20	1.18	65.69	
3	RuS_2		1.51	0.71	<LD	<LD	0.74	55.16	3.23	1.27	37.57	100.19
			1.51	0.62	<LD	<LD	0.39	30.46	0.94	0.69	65.4	
4	RuS_2	Figure 5b	4.83	3.39	<LD	<LD	<LD	44.72	9.08	1.9	37.09	101.01
			4.79	2.96	<LD	<LD	<LD	24.51	2.62	1.02	64.10	
5	RuS_2		2.96	1.37	<LD	<LD	<LD	53.10	4.56	1.46	37.91	101.36
			2.91	1.18	<LD	<LD	<LD	28.86	1.30	0.78	64.96	
6	RuS_{2+x}	Figure 5c	3.67	1.88	<LD	<LD	0.61	31.88	20.05	5.94	37.76	101.79
			3.74	1.68	<LD	<LD	0.33	17.96	5.94	3.29	67.06	
7	RuS_{2+x}		3.38	1.47	<LD	<LD	<LD	31.51	20.76	6.08	37.70	100.91
			3.48	1.33	<LD	<LD	<LD	17.93	6.21	3.40	67.64	
8	RuS_{2+x}		3.19	1.42	0.38	<LD	<LD	31.40	21.39	6.43	37.83	102.04
			3.27	1.28	0.20	<LD	<LD	17.78	6.37	3.58	67.53	
9	RuS_{2+x}		3.06	1.34	0.48	<LD	<LD	30.82	21.14	5.85	37.59	100.29
			3.18	1.22	0.26	<LD	<LD	17.68	6.38	3.30	67.99	
10	RuS_{2+x}		3.12	1.45	<LD	<LD	<LD	31.16	21.74	5.97	38.10	101.53
			3.20	1.31	<LD	<LD	<LD	17.65	6.48	3.32	68.04	
11	RuS_{2+x}		3.62	1.56	<LD	<LD	<LD	31.79	20.03	6.01	38.16	101.17
			3.69	1.4	<LD	<LD	<LD	17.90	5.93	3.32	67.75	
12	RuS_{2+x}		2.09	1.20	0.43	<LD	0.57	53.25	4.30	1.46	37.88	101.18
			2.07	1.04	0.22	<LD	0.30	29.10	1.24	0.78	65.26	
13	RuS_{2+x}		3.46	1.51	<LD	<LD	<LD	37.21	14.01	6.11	38.24	100.55
			3.48	1.34	<LD	<LD	<LD	20.7	4.10	3.34	67.05	
14	(Rh, Ir, Ru) $_3\text{S}_8$	Figure 5e	3.22	1.83	<LD	<LD	<LD	18.75	20.19	17.59	40.87	102.46
			3.16	1.58	<LD	<LD	<LD	10.18	5.76	9.38	69.94	
15	(Rh, Ir, Ru) $_3\text{S}_8$		3.07	1.81	<LD	<LD	<LD	18.4	20.39	17.8	40.33	101.79
			3.05	1.58	<LD	<LD	<LD	10.1	5.89	9.60	69.79	
16	(Rh, Ir, Ru) $_3\text{S}_8$		3.49	2.99	0.46	<LD	<LD	12.61	18.22	23.6	41.49	102.85
			3.37	2.53	0.23	<LD	<LD	6.72	5.11	12.35	69.70	
17	(Rh, Ir, Ru) $_3\text{S}_8$		3.10	2.24	<LD	<LD	<LD	14.13	19.65	21.56	40.77	101.45
			3.06	1.94	<LD	<LD	<LD	7.71	5.64	11.55	70.10	
18	(Rh, Ir, Ru) $_3\text{S}_8$		3.20	2.63	<LD	<LD	<LD	13.65	19.18	21.71	40.63	101.00
			3.16	2.28	<LD	<LD	<LD	7.45	5.51	11.64	69.95	
19	(Rh, Ir, Ru) $_3\text{S}_8$	Figure 5f	2.77	3.10	<LD	<LD	<LD	6.71	19.02	29.25	41.12	101.96
			2.71	2.66	<LD	<LD	<LD	3.63	5.41	15.53	70.07	
20	(Rh, Ir, Ru) $_3\text{S}_8$		3.72	3.92	<LD	<LD	<LD	3.20	15.23	32.20	41.81	100.08
			3.59	3.32	<LD	<LD	<LD	1.71	4.27	16.86	70.26	
21	(Rh, Ir, Ru) $_3\text{S}_8$	Figure 5g	2.59	5.76	<LD	<LD	<LD	<LD	4.09	43.66	43.78	99.89
			2.38	4.65	<LD	<LD	<LD	<LD	1.09	21.78	70.10	
22	$\text{Cu}_x\text{RhS}_{-3}$	Figure 5h	2.64	5.70	<LD	<LD	<LD	<LD	4.09	43.97	43.12	99.54
			2.45	4.65	<LD	<LD	<LD	<LD	1.10	22.13	69.67	
23	(Cu, Fe) $_{-2}(\text{Pt}, \text{Rh})_1\text{S}_{-5}$		5.04	20.28	<LD	33.09	1.09	<LD	<LD	2.28	33.10	94.87
			5.49	19.41	<LD	10.32	0.62	<LD	<LD	1.35	62.81	
24	(Cu, Fe) $_{-2}(\text{Pt}, \text{Rh})_1\text{S}_{-5}$		4.13	17.14	<LD	39.10	<LD	<LD	<LD	2.95	30.56	93.88
			4.85	17.68	<LD	13.13	<LD	<LD	<LD	1.88	62.47	

¹ For each phase, compositions expressed in wt. % (first row) and in mol. % (second row). ² Detection limit, LD, was 0.4–0.5 wt. % for Pt, and 0.1–0.2 wt. % for the others. For all phases with 0.5–2 μm of size, reliability of the composition determination was based on the analysis of 5–20 individual inclusions being identical in color, luster, and shape, and preference was given to measurements on the largest crystals.

In addition to Ru-crystals, the *Iss* + *Bnss* matrix also contains elongated oriented (Rh, Ir)₃S₈ inclusions up to 1 × 10 μm in size, which form colonies (Figure 5h) and single irregularly shaped grains of about 3 × 2 μm in size, which were bordered by the phase (Cu, Fe)_{−2}(Pt, Rh)₁S_{−5} (Figure 5g). The rough inclusions, unlike crystals, do not dissolve Ru, and we believe that they can occur both in the solidification process and as a result of solid-phase processes. At the moment, we have no idea about the real mechanism of their formation, although the second mechanism appears more preferable.

The Rh-S system in the sulfur-rich region (>60 at. %) is known only as hypothetical. In this region, below a temperature of ~757 °C, the cubic sulfide RhS_{−3} is stable [49]. In [53] the existence of a phase compositionally close to Rh₃S₈ was shown. The phase diagrams of the ternary systems Rh-Fe-S (at 900 and 500 °C) and Rh-Cu-S (at 900, 700 and 500 °C) were studied in [54,55]. Based on them, a phase Rh_{2.75}S_{7.25} with 4 at. % Fe occurs in the Rh-Fe-S system, whereas in the Rh-Cu-S system at a temperature of 900 °C, the solid solution Cu_xRhS_{3x} (*x* varies from 11.3 to 5.1 at. %), and RhS_{−3} (with 1.8 at. % Cu) is stable. At a temperature of 700 °C, the range of solid solution Cu_xRhS_{3x} changes from Cu_{16.0}Rh_{16.3}S_{67.7} to Cu_{14.89}Rh_{28.6}S_{56.6}, whereas “RhS_{−3}” phase has a composition rich in copper Cu_{2.4}Rh_{25.5}S_{72.7}.

Pt, Pd, Au, Ag. Our experiment showed that Pt, Pd, Au, and Ag form their own phases at the tail of the ingot (*g* ≥ 0.86). Ag, Au*, PdS, the phase ~Rh₃S₈, and an unnamed phase (Cu, Fe)_{−2}(Pt, Rh)₁S_{−5} were found in this area. Micron inclusions of these phases show a tendency to faceting (Figure 6a–f), although uncut individual inclusions are also found (Figure 6g,h).

Palladium forms the phase Pd_{0.97}Cu_{0.04}S, which is similar to the vysotskite mineral but contains an admixture of Cu. It is present in bornite as faceted crystals about 1 × 1 μm in size in the *Bnss* matrix (Figure 6d), but more often, its grains form intergrowths of Pd_{0.97}Cu_{0.04}S/Au* in the matrix *Iss* + *Bnss* (Figure 6c). In [55], it was shown that up to 1 at. % Cu can be dissolved in PdS. The Au* alloy contains ~84 at. % Au, ~13 at. % Ag, and several percentages of Cu and Fe. The main part of Au* inclusions, its two-phase intergrowths with Ag, PdS, and Cu-Pt-sulfide phase are related to *Bnss* (Figure 6b–d,g–i). Silver with an impurity of ~2 at. % Cu that were single-phase faceted inclusions up to 4 × 4 μm in size and two-phase aggregates Ag/Au* were found in the *Bnss* matrix (Figure 6a,h). In addition, *Iss* grains were turned by Ag (Figure 6f). The presence of impurities in Au* and Ag was possible, since solid solutions of Ag, Cu, Fe with Au, and Ag with Cu are formed on the melting diagrams of binary Au-Ag, Au-Cu, Au-Fe, and Ag-Cu systems [49]. Platinum forms the (Cu, Fe)_{−2}(Pt, Rh)₁S_{−5} phase with the composition Cu_{19.0±1.8}Fe_{4.9±0.1}Pt_{11.7±2.0}Rh_{1.7±0.4}S_{62.7±0.2} (Table 2). It may contain ~0.6 at. % Pd as impurity.

This phase occurred in the Fe-Cu sulfide matrix as single grains prone to faceting, as clusters of irregular shape ranging in size from <1 μm to 2 × 10 μm, as rims around the grains of the Rh₃S₈ phase (Figure 6e,f), and as intergrowths with Au* (Figure 6i). There are no data in the literature on the phase diagram of the Cu-Pt-S ternary system and systems of higher component content, and thus, reliable phase identification of this phase presents difficulties.

Summing up of all the experiments, one can advance that entering of noble metals in the matrix sulfide has a minor effect on crystallization of macrocomponent sulfide phases [56]. Noble metals are deposited mainly as sulfide compounds, exclusive of gold and silver, which are in a metallic state and occur also as solid solution (see Figure 6h). They might occur in the cooled ingot due to the crystallization process, and as solid-phase decay of parental sulfide and their low-sized particles remain invisible for XRD analysis.

3.2.2. Raman Spectra of Ru-Rh-Ir Sulfide

Raman spectra of Ru-Rh-Ir sulfide samples presented by typical experimental spectrum 1 (RuS₂ laurite-like) and calculated spectrum 2 are shown in Figure 7. The conventional cell of RuS₂ [57] consists of 12 atoms that results in 36 vibrational modes. The total set of irreducible representations [58] should be written as $\Gamma_{\text{vibr}} = A_g + 2A_u + E_g + 2E_u + 6T_u + 3T_g$, where non-degenerate is *A_g* and *A_u*, doubly degenerate is *E_g* and *E_u*, and triply degenerate is *T_u* and *T_g*.

One of the T_u modes is acoustical, while the remaining T_u modes are infrared-active. The Raman-active modes are $A_g + E_g + 3T_g$, and the A_u and E_u are silent modes. The DFT-calculated Raman spectra for RuS₂ are shown in Figure 7 (2–5). Spectral contours were simulated with Lorentzian broadening, equal to 5, 10, and 20 cm^{−1} and, as can be seen in Figure 7 (2–4), excellent agreement with experimental data (1) was achieved using 20 cm^{−1} broadening. Probably, this band widening is caused by low-size crystallinity and some variation of Ru-Rh-Ir composition at the volume of accumulation of Raman signal (2 μm × 2 μm × 20 μm).

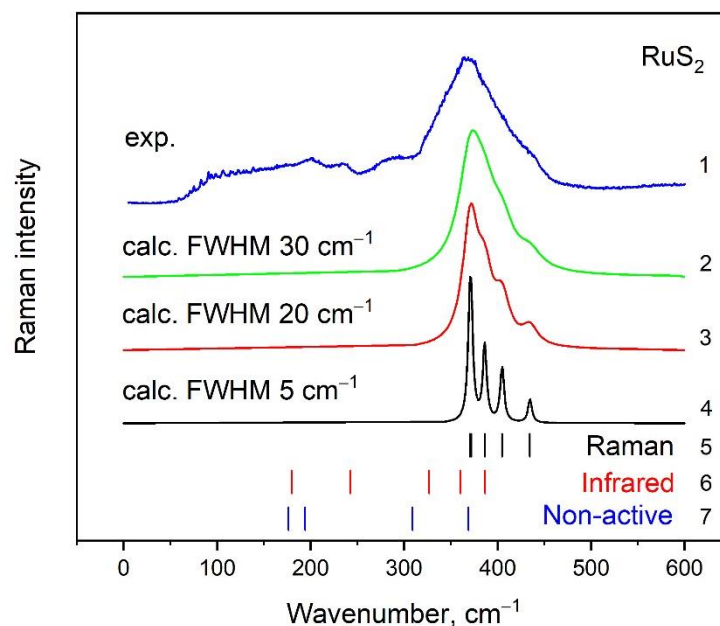


Figure 7. Experimental (1) and calculated (2–4) Raman spectra of RuS₂ (laurite structure). Calculated dashed spectral diagrams (5–7) are presented, including Raman-active (5), infrared-active (6), and non-active (7) vibrational modes. Calculated Raman spectra (2–4) are plotted using different bandwidths (FWHM): 5 (4), 20 (3), and 30 (2) cm^{−1}.

The crystal structure of RuS₂ consists of octahedral RuS₆ units connected through common vertices and through S-S bridges. Experimental high intensity peak around 368 cm^{−1} is a combination of two vibrations. The first one is related to S-Ru-S stretching mixed with the rotation of S ions around the S-Ru-S axis, see Figure 8a, and the second one is an antiphase stretching of S-Ru-S in neighboring octahedral groups, as shown in Figure 8b. Due to the fact that the octahedral groups are interconnected, vibrations of structural units take on a complex form and should not be described only as RuS₆ vibrations. Thus, the S-S stretching vibrations formally lead to rotations of RuS₆, shown by red arrows in Figure 8c. The triply degenerated T_g mode with calculated wavenumber equal to 404.9 cm^{−1} is an opposite sulfur vibration, as shown in Figure 8d. The calculated vibrational mode with the highest wavenumber value is a triply degenerated (T_g) vibration of sulfur ions in crystal planes, as shown in Figure 8e.

Calculated phonon dispersion curves $v(k)$ (the band frequency versus the wave vector) within the Brillouin zone of RuS₂ laurite structure are plotted in Figure 9. Recently [59], phonon dispersion was modeled for new marcasite phase of RuS₂ and for p-RuS₂ (laurite) structure at 8 GPa; however, not every path through high symmetry points of BZ was presented. The full path along the Brillouin zone points should be chosen as Γ -X-M- Γ -R-X, R-M-X₁ and coordinates of these points are $\Gamma(0,0,0)$, X(0,0.5,0), M(0.5,0.5,0), R(0.5,0.5,0.5), X₁(0.5,0,0) [60]. As can be seen in Figure 9, there are no imaginary phonon modes over the whole Brillouin zone; thus, the investigated structure is dynamically stable. The range from 350 to 450 cm^{−1} at the Γ -point was studied experimentally with Raman spectroscopy method and discussed above. Remain vibrational (infrared-active and silent modes) modes in the center of BZ are from 150 to 400 cm^{−1}. At the same time, due to the imperfection of the crystal structure (impurities, disordering, etc.), one should not exclude the possibility

of the appearance of phonons from other points of BZ in the experimental Raman spectra. Thus, the appearance of wide spectral bands below 350 cm^{-1} in Figure 9 can be possibly explained due to the imperfection of laurite crystal structure, in addition.

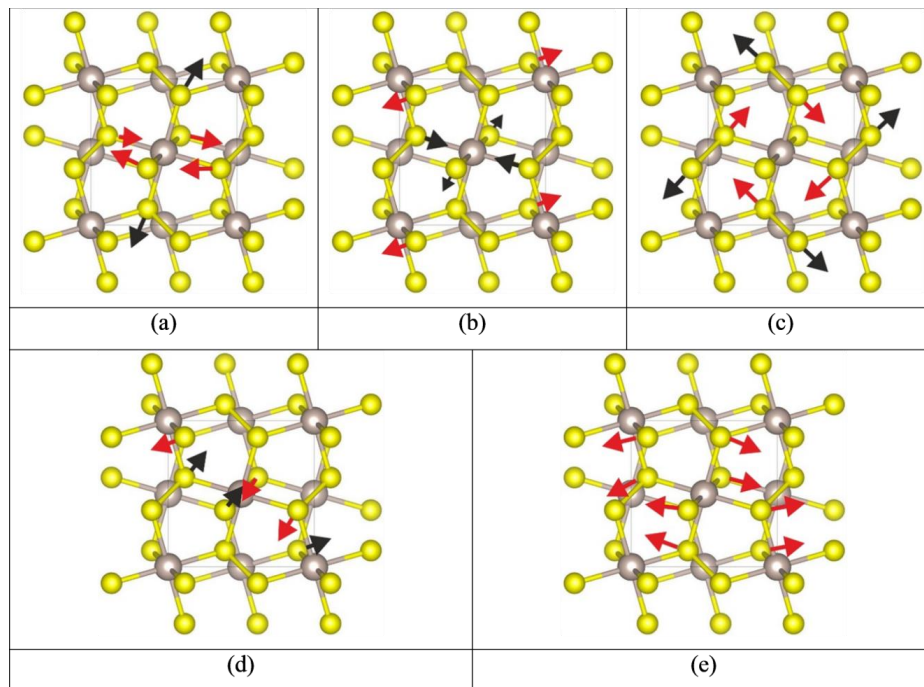


Figure 8. Schematic representation of vibrational modes: (a) E_g 370.5 cm^{-1} , (b) T_g 372.1 cm^{-1} , (c) A_g 386.8 cm^{-1} , (d) T_g 404.9 cm^{-1} , (e) T_g 434.7 cm^{-1} .

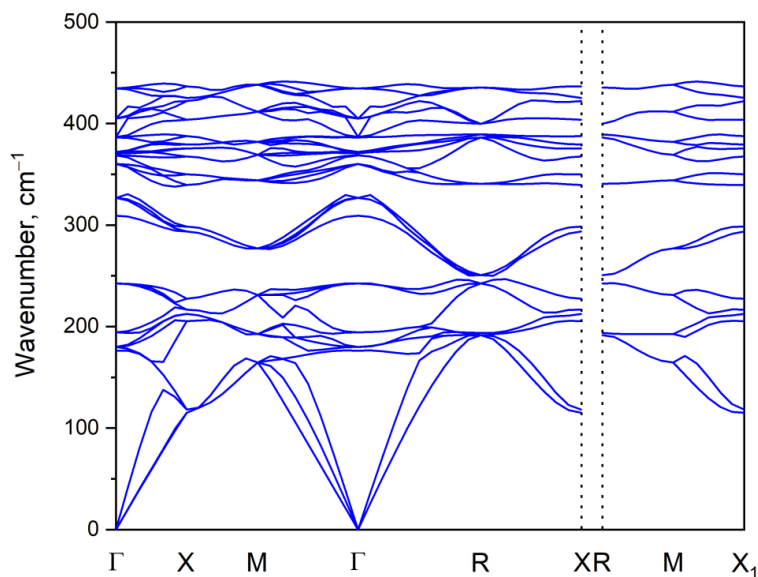


Figure 9. Ab initio calculated phonon dispersion curves of the Brillouin zone of RuS_2 laurite structure plotted along major directions.

Figure 10 shows experimental Raman spectrum of the sample $(\text{Ir, Rh, Ru})_3\text{S}_8$, compared with the calculated Raman spectra (dashed spectral diagrams) of idealized phases of structure type-II: Ru_3S_8 , Rh_3S_8 , and Ir_3S_8 .

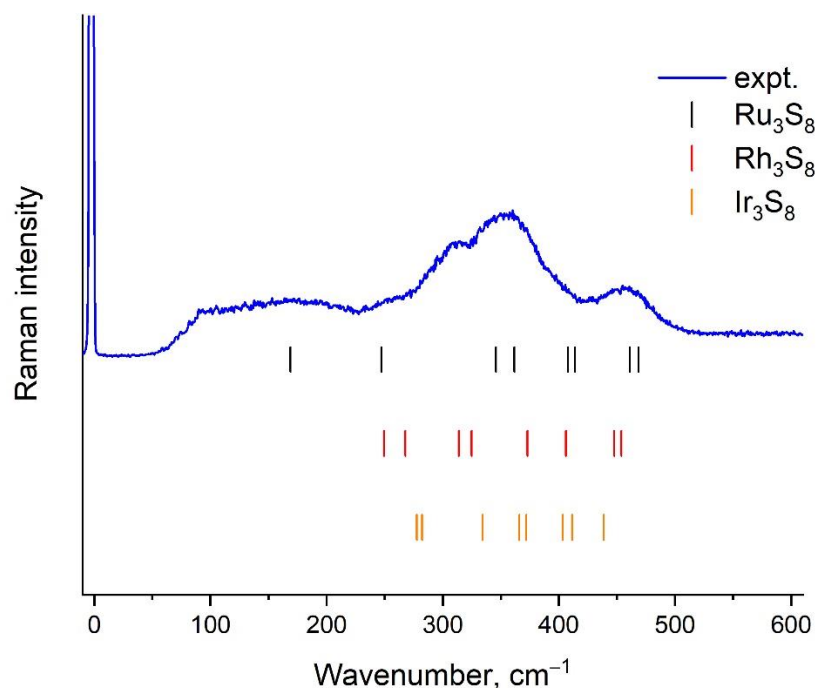


Figure 10. Experimental (blue spectrum) Raman spectrum of the sample $(\text{Rh, Ir, Ru})_3\text{S}_8$ and calculated dashed spectral diagrams of Ru_3S_8 (black), Rh_3S_8 (red), and Ir_3S_8 (orange).

There is satisfactory correspondence of the three calculated spectra to the experimental one. It does not seem possible to give preference to one of the three idealized structures and to one Raman spectrum of this phase.

For poorly structurally attested cation-mixed Ru-Rh-Ir sulfide, interpretation of the Raman spectra (A_g , E_g and T_g modes) is presented, based on ab initio calculations of the crystal structure, electronic band structure, and lattice dynamics, together with the calculated forms of vibrations of all bands observed in Raman spectra. The IR spectrum (T_u modes) and the set of inactive vibrations (A_u and E_u modes, which are forbidden in the IR and Raman spectra) are also presented. Using ab initio lattice dynamics calculations, the Raman spectra of the mixed (Ir, Ru, Rh) sulfide with the Ir_3S_8 type of structure are interpreted for the first time.

3.2.3. Features of the Behavior of Microcomponents

Noble metals form individual phases during the directional crystallization of the ingot. Enrichment of the melt in copper and sulfur during crystallization exerts influence on the sequence of phase occurrence along the ingot length. An increase in sulfidization degree in Ru, Rh, and Ir is observed during crystallization. Therefore, at the beginning of the process in zone I, stoichiometric laurite RuS_2 is predominantly formed, doped with Ir and Rh up to 1 at. %, but with increasing g it is transformed at first to sulfur-rich laurite $(\text{Ru, Rh, Ir})\text{S}_{2+x}$, enriched with Ir and Rh (up to 6 at. %), and then it is rich in sulfur and Rh phase $(\text{Rh, Ir, Ru})_3\text{S}_8$. At the end of the process in zone II, the following noble metal sulfides are formed: $(\text{Rh, Ir})_3\text{S}_8$, Rh_3S_8 , PdS , and a phase rich in copper and platinum $(\text{Cu, Fe})_{-2}(\text{Pt, Rh})_1\text{S}_{-5}$. For gold and silver, only metal mineral molds were detected. Note the complex behavior of rhodium during the crystallization of a zonal sample. In zone I, it dissolves in RuS_2 , and being left in the melt, Rh noticeably accumulates in the melt and then forms the $(\text{Rh, Ir, Ru})_3\text{S}_8$ phase. By the end of the process in zone II, Rh completely replaces Ru and Ir in this phase and also dissolves in the phase $(\text{Cu, Fe})_{-2}(\text{Pt, Rh})_1\text{S}_{-5}$. The $(\text{Rh, Ir, Ru})_3\text{S}_8$ sulfide remains as a poorly structurally attested phase since the structural data are known only for the stoichiometric compound in the Ir_3S_8 phase.

Features of the behavior of impurity components forming independent microphases were considered in the context of the theory of directional crystallization of multicomponent

melts presented in [61]. In the presence of noble metal additives, the zoning of platinum group elements (PGE), Au, and Ag impurities is superimposed on the zonal distribution of the main components. Each impurity zone differs in that it has its own set of microphases. The transition from one zone to another leads to disappearance or occurrence of a new microphase that occurs more often. As a result, a regular change in the microphases distribution along the ingot length should occur. In our ingot, such a strict regularity is not observed. Nevertheless, one can observe fractionation of elements with distribution coefficients solid/liquid >1 (Ru, Ir, and Rh) and <1 (Pt, Pd, Au, and Ag). Therefore, the first portions of the sulfide melt are enriched in Ru, Ir, and Rh, while the last portions of the melt are enriched in sulfur and copper, and concentrate elements Pt, Pd, Au, and Ag. They are deposited from the melt, respectively, at the initial or final stage of ingot formation as a combination of minerals of these elements. Due to the small amount of microcomponents, a solid crystallization front cannot form. Therefore, the formation of nuclei becomes the main limiting stage, and the nuclei formation goes under highly non-equilibrium conditions. Thus, we can state that, in this case, the theory of quasi-equilibrium directional crystallization for microcomponents does not function, as was noted by us previously in [22–26].

It is known that the Cu-Fe-S system, including noble elements, is the basic geochemical system and is widely used to model the formation of sulfide igneous ores of copper and nickel, and to interpret geochemical and mineralogical data. A significant lack of information about the phase relationships in such a complex system does not allow for the explanation of the physicochemical features of the formation of massive ore bodies. In this case, the directional crystallization method makes it possible, because an ingot was obtained which imitates the zoning of a solid sulfide ores body, providing fresh insight into the behavior of noble metals in this process. Knowledge of the ideal equilibrium behavior of the impurity phases allows for the more reliable interpretation of their non-equilibrium transformations depending on temperature. In our study, an interesting fact was obtained: Ru, Rh, and Ir form sulfide phases, while the Au and Ag metals remain uncombined. This is consistent with known mineralogical data that ruthenium sulfide laurite RuS_2 is widespread in copper-rich paragenesis, while gold forms Au alloys with Ag and Cu.

4. Conclusions

A large amount of new quantitative information was obtained in the work regarding a fragment of the phase diagram of the Cu-Fe-S system in the region important for the formation of copper-rich and sulfur-rich sulfide ores. Acquisition of this new knowledge was made possible due to the combination of a specific unconventional method of directional crystallization of the melt and traditional synthetic and characterization methods.

Regions of primary crystallization of *Iss* and *Ls* in the tested region of the diagram were established, and this is quite consistent with the constitution of the melting diagram of the Cu-Fe-S system, and the *Iss* fraction of the initial part of the ingot comes to 91 vol. %. The distribution curves of the components in the ingot are constructed, which correspond to the primary zoning. The constructed distribution curves showed that the first portions of *Iss* crystallized from the melt are enriched in Fe and depleted in S, relative to the initial melt. The coefficients of the interfacial distribution of Cu, Fe, and S, and the liquidus temperature along the crystallization path, were determined and, based on them, the liquidus and solidus lines were also constructed. The secondary mineral zoning formed during subsolidus transformations of primary phases such as $Iss^t + Cp^t$, $Iss^t + Cp^t$ and $Iss + Bn + Chc + Id$, was determined, and such zoning can present in natural Cu-rich sulfide ores.

The regularities of the behavior of Pt, Pd, Rh, Ru, Ir, Au, and Ag during the fractional crystallization of the melt were studied. During crystallization, the first portions of the melt were enriched in Ru, Ir, and Rh, while the last portions of the melt were enriched in sulfur and copper and concentrate from elements Pt, Pd, Au, and Ag or Ru, while Rh and Ir increased the sulfidization. They are deposited from the melt, respectively, in the initial

or final stage of ingot formation as a combination of minerals of these elements. Their formation proceeds through the stage of nucleation and growth of microcrystals.

Using ab initio lattice dynamics calculations, the Raman spectra of the mixed (Ir, Ru, Rh) sulfide with an Ir₃S₈ type of structure are interpreted for the first time.

Author Contributions: E.F.S. conceptualization, performed the experiments, interpreted the results, and wrote the paper; A.S.O. and S.V.G.—Raman method; I.G.V. interpreted the results, and wrote and edited the paper; N.S.K. analyzed the compositions of phases; all the authors participated in the manuscript preparation. All authors have read and agreed to the published version of the manuscript.

Funding: This work was supported by the Russian Federation state assignment of Sobolev Institute of Geology and Mineralogy of SB RAS, Nikolaev Institute of Inorganic Chemistry SB RAS, and Kirensky Institute of Physics of Federal Research Center KSC SB RAS. The grant number is projects II.1.64. and 40330-2016-0001.

Acknowledgments: The authors thank K. A. Kokh for the help in the work.

Conflicts of Interest: The authors declare no conflict of interest.

References

- Schlegel, H.; Sehüller, A. Das Zustandebild Kupfer-Eisen-Schwefel. *Z. Met.* **1952**, *43*, 421–428.
- Greig, J.W.; Jensen, E.; Mervn, H.E. The system Cu-Fe-S. *Carnegie Inst. Wash. Yearb.* **1955**, *54*, 129–134.
- Kullerud, G.; Yund, R.A.; Moh, G.H. Phase relations in the Cu-Fe-S, Cu-Ni-S, and Fe-Ni-S systems magmatic ore deposits. *Econ. Geol. Monogr.* **1969**, *4*, 323–343.
- Tsujimura, T.; Kitakaze, A. New phase relations in the Cu-Fe-S system at 800 °C. Constraint of fractional crystallization of a sulfide liquid. *Neues Jahrb. Für Mineral.* **2004**, *10*, 433–444. [[CrossRef](#)]
- Kosyakov, V.I. Topological analysis of the melting diagram of the Cu-Fe-S system. *Russ. J. Inorg. Chem.* **2008**, *53*, 946–951. [[CrossRef](#)]
- Kitakaze, A. Phase relation of some sulfide systems-(4) Especially Cu-Fe-S system. *Mem. Fac. Eng. Yamaguchi Univ.* **2017**, *68*, 23–39.
- Kosyakov, V.I.; Sinyakova, E.F. Melt Crystallization of CuFe₂S₃ in the Cu-Fe-S system. *J. Therm. Anal. Calorim.* **2014**, *115*, 511–516. [[CrossRef](#)]
- Kosyakov, V.I.; Sinyakova, E.F. Study of crystallization of nonstoichiometric isocubanite Cu_{1.1}Fe_{2.0}S_{3.0} from melt in the system Cu-Fe-S. *J. Therm. Anal. Calorim.* **2017**, *129*, 623–628. [[CrossRef](#)]
- Sinyakova, E.F.; Kosyakov, V.I. Experimental modeling of zonality of copper-rich sulfide ores in copper-nickel deposits. *Dokl. Earth Sci.* **2009**, *427*, 787–792. [[CrossRef](#)]
- Cabri, L.J. New data on phase relations in the Cu-Fe-S system. *Econ. Geol.* **1973**, *68*, 443–454. [[CrossRef](#)]
- Naldrett, A.J. *Magmatic Sulfide Deposits: Geology, Geochemistry and Exploration*; Springer: Berlin, Germany, 2004; p. 727.
- Distler, V.V. Platinum mineralization of the Noril'sk deposits. In *Geology and Genesis of Platinoid Deposits*; Nauka: Moscow, Russia, 1994; pp. 7–35. (In Russian)
- Barnes, S.-J.; Ripley, E.M. Highly siderophile and strongly chalcophile elements in magmatic ore deposits. *Rev. Mineral. Geochem.* **2016**, *81*, 725–774. [[CrossRef](#)]
- Czamanske, G.K.; Kunilov, V.E.; Zientek, M.L.; Cabri, L.J.; Likchachev, A.P.; Calk, L.C.; Oscarson, R. A proton-microprobe study of magmatic sulfide ores from the Noril'sk-Talnakh district, Siberia. *Can. Mineral.* **1992**, *30*, 249–287.
- Duran, C.J.; Barnes, S.-J.; Pleše, P.; Prašek, M.K.; Zientek, M.L.; Pagé, P. Fractional crystallization-induced variations in sulfides from the Noril'sk-Talnakh mining district (polar Siberia, Russia). *Ore Geol. Rev.* **2017**, *90*, 326–351. [[CrossRef](#)]
- Dare, S.A.S.; Barnes, S.-J.; Prichard, H.M.; Fisher, P.C. Mineralogy and geochemistry of Cu-Rich ores from the McCreey East Ni-Cu-PGE deposit (Sudbury, Canada): Implications for the behavior of platinum group and chalcophile elements at the end of crystallization of a sulfide liquid. *Econ. Geol.* **2014**, *109*, 343–366. [[CrossRef](#)]
- Simon, G.; Kesler, S.E.; Essene, E.J. Gold in Porphyry Copper Deposits: Experimental Determination of the Distribution of Gold in the Cu-Fe-S System at 400 to 700 °C. *Econ. Geol.* **2000**, *95*, 259–270. [[CrossRef](#)]
- Peregoedova, A.; Ohnenstetter, M. Collectors of Pt, Pd and Rh in a S-poor Fe-Ni-Cu sulfide system at 760 °C: Experimental data and application to ore deposits. *Can. Mineral.* **2002**, *40*, 527–561. [[CrossRef](#)]
- Peregoedova, A.; Barnes, S.-J.; Baker, D.R. The formation of Pt-Ir alloys and Cu-Pd-rich sulfide melts by partial desulfurization of Fe-Ni-Cu sulfides: Results of experiments and implications for natural systems. *Chem. Geol.* **2004**, *208*, 247–264. [[CrossRef](#)]
- Helmy, H.M.; Ballhaus, C.; Fonseca, R.O.C.; Wirth, R.; Nagel, T.J.; Tredoux, M. Noble metal nanoclusters and nanoparticles precede mineral formation in magmatic sulfide melts. *Nat. Commun.* **2013**, *4*, 2405. [[CrossRef](#)] [[PubMed](#)]
- Cafagna, F.; Jugo, P.J. An experimental study on the geochemical behavior of highly siderophile elements (HSE) and metalloids (As, Se, Sb, Te, Bi) in a mss-iss-pyrite system at 650 °C: A possible magmatic origin for Co-HSE-bearing pyrite and the role of metalloid-rich phases in the fractionation of HSE. *Geochim. Cosmochim. Acta* **2016**, *178*, 233–258.

22. Distler, V.V.; Sinyakova, E.F.; Kosyakov, V.I. Behavior of noble metals upon fractional crystallization of copper-rich sulfide melts. *Dokl. Earth Sci.* **2016**, *469*, 811–814. [CrossRef]
23. Sinyakova, E.; Kosyakov, V.; Distler, V.; Karmanov, N. Behavior of Pt, Pd, and Au during crystallization of Cu-rich magmatic sulfides. *Can. Mineral.* **2016**, *54*, 491–509. [CrossRef]
24. Sinyakova, E.F.; Kosyakov, V.I.; Goryachev, N.A. Formation of drop-shaped inclusions based on Pt, Pd, Au, Ag, Bi, Sb, Te, and As under crystallization of an intermediate solid solution in the Cu–Fe–Ni–S system. *Dokl. Earth Sci.* **2019**, *489*, 1301–1305. [CrossRef]
25. Sinyakova, E.F.; Kosyakov, V.I.; Borisenko, A.S.; Karmanov, N.S. Behavior of noble metals during fractional crystallization of Cu–Fe–Ni–(Pt, Pd, Rh, Ir, Ru, Ag, Au, Te) sulfide melts. *Russ. Geol. Geophys.* **2019**, *60*, 642–651. [CrossRef]
26. Sinyakova, E.; Kosyakov, V.; Palyanova, G.; Karmanov, N. Experimental modeling of noble and chalcophile elements fractionation during solidification of Cu–Fe–Ni–S melt. *Minerals* **2019**, *9*, 531. [CrossRef]
27. Vaughan, D.J.; Craig, J.R. *Mineral Chemistry of Metal Sulfides*, Cambridge Earth Science Series; Cambridge University Press: Cambridge, UK, 1978; p. 493.
28. Kosyakov, V.I.; Sinyakova, E.F. Directional crystallization of Fe–Ni sulfide melts within the crystallization field of monosulfide solid solution. *Geochem. Int.* **2005**, *43*, 372–385.
29. Flemings, M.C. *Solidification Processing*; McGraw-Hill Book Company: New York, NY, USA, 1974; p. 423.
30. Mackenzie, R.C. Basic principles and historical development. In *Differential Thermal Analysis; Fundamental Aspects*; Academic Press: London, UK; New York, NY, USA, 1970; pp. 3–30.
31. Likhacheva, A.Y.; Goryainov, S.V.; Rashchenko, S.V.; Dementiev, S.N.; Safonov, O.G. In situ observation of chrysotile decomposition in the presence of NaCl-bearing aqueous fluid up to 5 GPa and 400 °C. *Mineral. Petrol.* **2021**, *115*, 213–222. [CrossRef]
32. Bakker, R.J. Application of Combined Raman Spectroscopy and Electron Probe Microanalysis to Identify Platinum Group Minerals. Available online: https://fluids.unileoben.ac.at/Publications_files/Bakker_EMAS.pdf (accessed on 1 August 2020).
33. Grishina, S.; Goryainov, S.; Oreshonkov, A.; Karmanov, N. Micro-Raman study of cesanite (Ca₂Na₃(OH)(SO₄)₃) in chloride segregations from Udachnaya-East kimberlites. *J. Raman Spectrosc.* **2021**, *52*, 497–507. [CrossRef]
34. Goryainov, S.V.; Krylova, S.N.; Borodina, U.O.; Krylov, A.S. Dynamical immiscibility of aqueous carbonate fluid in the shortite–water system at high-pressure–temperature conditions. *J. Phys. Chem. C* **2021**, *125*, 18501–18509. [CrossRef]
35. Model S506 Interactive Peak Fit User’s Manual. 2002. Available online: <http://depni.sinp.msu.ru/~hatta/canberra/S506%20Interactive%20Peak%20Fit%20User%27s%20Manual.pdf> (accessed on 1 August 2022).
36. Hohenberg, P.; Kohn, W. Inhomogeneous electron. *Gas. Phys. Rev.* **1964**, *136*, B864–B871. [CrossRef]
37. Kohn, W.; Sham, L.J. Self-consistent equations including exchange and correlation effects. *Phys. Rev.* **1965**, *140*, A1133–A1138. [CrossRef]
38. Oreshonkov, A.S. SI: Advances in density functional theory (DFT) studies of solids. *Materials* **2022**, *15*, 2099. [CrossRef]
39. Clark, S.J.; Segall, M.D.; Pickard, C.J.; Hasnip, P.J.; Probert, M.I.J.; Refson, K.; Payne, M.C. First principles methods using CASTEP. *Z. Für Krist.* **2005**, *220*, 567–570. [CrossRef]
40. Srivastava, G.P.; Weaire, D. The theory of the cohesive energies of solids. *Adv. Phys.* **1987**, *36*, 463–517. [CrossRef]
41. Baroni, S.; Gironcoli, S.; Corso, A.D.; Gianozzi, P. Phonons and related crystal properties from density-functional perturbation theory. *Rev. Mod. Phys.* **2001**, *73*, 515–562. [CrossRef]
42. Kosyakov, V.I.; Sinyakova, E.F. Physicochemical prerequisites for the formation of primary orebody zoning at copper-nickel sulfide deposits (by the example of the systems Fe–Ni–S and Cu–Fe–S). *Russ. Geol. Geophys.* **2012**, *53*, 861–882. [CrossRef]
43. Sinyakova, E.F.; Kosyakov, V.I. The section of the Fe–Ni–S phase diagram constructed by directional crystallization and thermal analysis. *J. Therm. Anal. Calorim.* **2013**, *111*, 71–76. [CrossRef]
44. Sinyakova, E.F.; Kosyakov, V.I. The polythermal section of the Cu–Fe–Ni–S phase diagram constructed using directional crystallization and thermal analysis. *J. Therm. Anal. Calorim.* **2014**, *117*, 1085–1089. [CrossRef]
45. Kosyakov, V.I.; Sinyakova, E.F.; Kokh, K.A. Sequential crystallization of four phases from melt on the polythermal section of the Cu–Fe–Ni–S system. *J. Therm. Anal. Calorim.* **2020**, *139*, 3377–3382. [CrossRef]
46. Sinyakova, E.F.; Komarov, V.Y.; Sopov, K.V.; Kosyakov, V.I.; Kokh, K.A. Crystallization of pyrrhotite from Fe–Ni–Cu–S–(Rh, Ru) melt. *J. Cryst. Growth* **2020**, *548*, 125822. [CrossRef]
47. Berry, L.G.; Thompson, R.M. *X-ray Powder Data for Ore Minerals: The Peacock Atlas*; Geological Society of America Memoir 85: New York, NY, USA, 1962; p. 281.
48. Kolonin, G.R.; Fedorova, Z.N.; Kravchenko, T.A. Influence of the composition of phase associations of the Cu–Fe–S system on the mineral forms of rhodium (according to experimental data). *Rep. Acad. Sci.* **1994**, *337*, 104–107.
49. Massalski, T.B.; Okamoto, H.; Subramanian, P.R.; Kacprzak, L. *Binary Alloy Phase Diagrams*, 2nd ed.; ASM International: Novelt, OH, USA, 1990; p. 3242.
50. Cabri, L.J. *The Geology, Geochemistry, Mineralogy and Mineral Beneficiation of Platinum-Group Elements*; Canadian Institute of Mining, Metallurgy and Petroleum: Montreal, QC, Canada, 2002; Volume 54, pp. 13–129.
51. Brenan, J.M.; Andrews, D. High-temperature stability of laurite and Ru–Os–Ir alloy and their role in PGE fractionation in mafic magmas. *Can. Mineral.* **2001**, *39*, 341–360. [CrossRef]
52. Andrews, D.R.A.; Brenan, J.M. Phase-equilibrium constraints of the magmatic origin of laurite + Ru–Os–Ir alloy. *Can. Mineral.* **2002**, *40*, 1705–1716. [CrossRef]
53. Kjekshus, A.; Rakke, T.; Andresen, A.F. Pyrite-like phases in the Rh–Te system. *Acta Chem. Scand.* **1978**, *A 32*, 209–217. [CrossRef]

54. Makovicky, E.; Makovicky, M.; Rose-Hansen, J. The system Fe–Rh–S at 900° and 500 °C. *Can. Mineral.* **2002**, *40*, 519–526. [[CrossRef](#)]
55. Makovicky, E. Ternary and quaternary phase systems with PGE. In *The Geology, Geochemistry, Mineralogy and Mineral Beneficiation of Platinum-Group Elements*; Canadian Institute of Mining, Metallurgy and Petroleum: Montreal, QC, Canada, 2002; Volume 54, pp. 131–175.
56. Ryabchikov, I.D. *Thermodynamic Analysis of the Behavior of Minor Elements during Crystallization of Silicate Melts*; Nauka: Moscow, Russia, 1965; p. 120. (In Russian)
57. Lutz, H.D.; Müller, B.; Schmidt, T.; Stingl, T. Structure refinement of pyrite-type ruthenium disulfide, RuS₂, and ruthenium diselenide, RuSe₂. *Acta Crystallogr. Sect. C* **1990**, *46*, 2003–2005. [[CrossRef](#)]
58. Aroyo, M.I.; Perez-Mato, J.M.; Orobengoa, D.; Tasci, E.; de la Flor, G.; Kirov, A. Crystallography online: Bilbao Crystallographic Server. *Bulg. Chem. Commun.* **2011**, *43*, 183–197.
59. Joshi, H.; Ram, M.; Limbu, N.; Rai, D.P.; Thapa, B.; Labar, K.; Laref, A.; Thapa, R.K.; Shankar, A. Modulation of optical absorption in m-Fe_{1-x}Ru_xS₂ and exploring stability in new m-RuS₂. *Sci. Rep.* **2021**, *11*, 6601. [[CrossRef](#)] [[PubMed](#)]
60. Hinuma, Y.; Pizzi, G.; Kumagai, Y.; Oba, F.; Tanaka, I. Band structure diagram paths based on crystallography. *Comp. Mater. Sci.* **2017**, *128*, 140–184. [[CrossRef](#)]
61. Kosyakov, V.I.; Sinyakova, E.F. Peculiarities of behavior of trace elements during fractional crystallization of sulfide magmas. *Dokl. Earth Sci.* **2015**, *460*, 179–182. [[CrossRef](#)]